CHAPTER 4

RAY COMPUTATION

Ray computation is the second stage of the ray tracing procedure and is composed of two steps. First, the normal to the current wavefront is computed. Then the intersection of this normal vector with the next wavefront is found. This process is repeated until the last wavefront is reached. For all examples shown here, the previous sample temporal correlation with first peak alignment correction method is used for wavefront reconstruction.

4.1 Normal Computation

The x and y values of the computational domain are assumed to be on a uniform spatial grid of $N \times N$ points separated by a distance $dx = dy$. The wavefront at a time t and position (x, y) will be denoted as $z(x, y, t)$. To compute the normal to the wavefront at a time t and x and y coordinates (x_0, y_0), first find the x and y coordinates on the computational grid that are closest to x_0 and y_0, respectively. This coordinate will be referred to as (x_q, y_q) and has corresponding wavefront value $z(x_q, y_q, t)$. The points surrounding (x_q, y_q) are then used to form four triangles, as shown in Fig. 4.1, where

$$P_{m,n} = (x_q, y_q, z(x_q, y_q, t)) \tag{4.1}$$

$$P_{m-1,n} = (x_q - dx, y_q, z(x_q - dx, y_q, t)) \tag{4.2}$$

$$P_{m,n-1} = (x_q, y_q - dy, z(x_q, y_q - dy, t)) \tag{4.3}$$

$$P_{m+1,n} = (x_q + dx, y_q, z(x_q + dx, y_q, t)) \tag{4.4}$$

$$P_{m,n+1} = (x_q, y_q + dy, z(x_q, y_q + dy, t)) \tag{4.5}$$

The normal is then computed by taking the cross product of two vectors

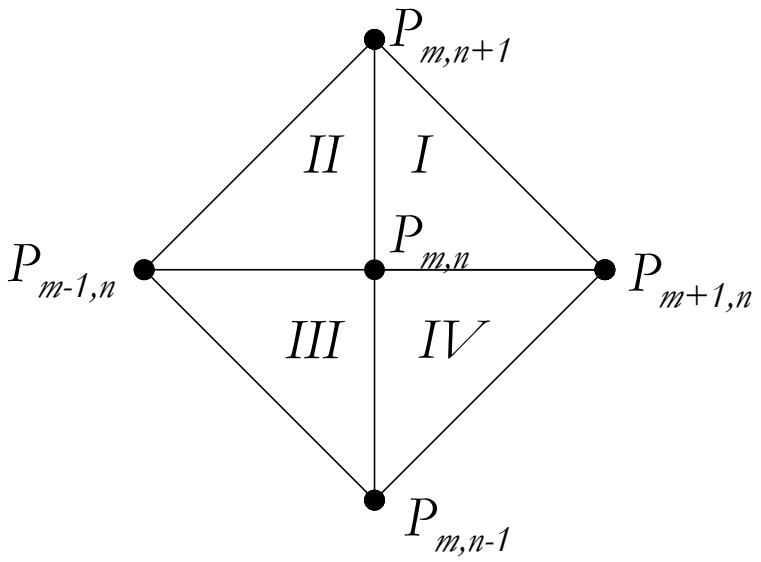

Figure 4.1: Triangles used to determine normal vector.

formed from the sides of the triangle containing $(x, y, z(x, y, t))$. For example if $(x, y, z(x, y, t))$ is located in triangle I, define $\mathbf{v_1} = P_{m+1,n} - P_{m,n}$ and $\mathbf{v_2} = P_{m,n-1} - P_{m,n}$. The normal vector $\mathbf{n}$ is then $\mathbf{v_1} \times \mathbf{v_2}$.

4.2 Intersection Computation

The intersection of the normal with the next wavefront is approximated by finding the intersection of the normal with a triangle formed by the discretized wavefront. Similar to what was done for the normal computation, the triangle closest to the intersection point must first be found. Let $(x_l, y_l, z(x_l, y_l, t))$ correspond to the wavefront at time t over the discretized domain. For all points over the domain find the vector $\mathbf{v_l}$ from the last intersection $(x_0, y_0, z(x_0, y_0, t))$ to each point on the next wavefront. The point which minimizes the magnitude of the error vector $\mathbf{e}$,

$$\mathbf{e} = \frac{\mathbf{n}}{|\mathbf{n}|} - \frac{\mathbf{v_l}}{|\mathbf{v_l}|} \tag{4.6}$$

is the point on the grid closest to the intersection and will be called $P_{m,n}$. The triangle containing the intersection is then found based on the direction of $\mathbf{e}$, similar to what was done for the normal computation. For example, if the

x component of $\mathbf{e}$ is positive and the y component of $\mathbf{e}$ is negative, triangle IV of Fig. 4.1 is used. The intersection of normal with the wavefront is then approximated as the intersection of the normal with this triangle. Let $a = (x_a, y_a, z_a)$, $b = (x_b, y_b, z_b)$, and $c = (x_c, y_c, z_c)$ be the three vertices of the triangle. The intersection of the normal with the wavefront is then [10]

$$(x_0 + n_x s, y_0 + n_y s, z_0 + n_z s) \tag{4.7}$$

where s can be found by solving the equation

$$\begin{bmatrix} x_0 - x_a \\ y_0 - y_a \\ z_0 - z_a \end{bmatrix} = \begin{bmatrix} -n_x & x_b - x_a & x_c - x_a \\ -n_y & y_b - y_a & y_c - y_a \\ -n_z & z_b - z_a & z_c - z_a \end{bmatrix} \begin{bmatrix} s \\ u \\ v \end{bmatrix} \tag{4.8}$$

4.3 Increasing Normal Accuracy

The discretization of the domain and resulting wavefronts result in normals computed from the wavefronts only being able to take on discrete directions. For example, consider the two dimensional case. The normal shown in Fig. 4.2(a) occurs when the wavefronts at x and $x + dx$ have the same value. The normal shown in Fig. 4.2(b) occurs when the wavefront at x is dz greater than the wavefront at $x + dx$. The normal shown in Fig. 4.2(c) occurs when the wavefront at x is $2dz$ greater than the wavefront at $x + dx$. This pattern can be repeated when the wavefront at x is mdz greater than the wavefront at $x + dx$, where m is an integer. Since propagation is assumed in the $+z$ direction, the normals shown in Figs. 4.2(a) and 4.2(b) occur most frequently. The normal should be able to take on any angle from 0 to 90° with respect to the x-axis but due to quantization it is only able to take on values of $\tan^{-1}(1/m)$. This can lead to significant error in ray tracing computations. A method of reducing this error is presented next.

One method of decreasing the error in the normal computation is to compute the arrival times rounded to an integer multiple of some sampling period T. Let the arrival time at position (x, y, z) be NT and the arrival time at position $(x, y, z + dz)$ be MT, where M and N are integers and $M > N$. One can then use linear interpolation of the wavefronts for the time intervals between. For example, let the arrival time at (x, y, z) be $8T$ and the

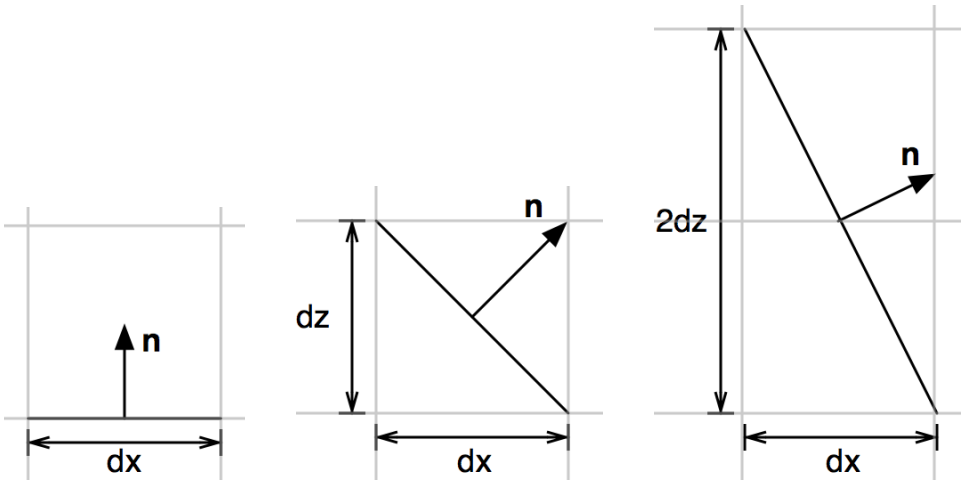

(a) $\mathbf{n} = \hat{z}$. (b) $\mathbf{n} = \hat{x} + \hat{z}$. (c) $\mathbf{n} = 2\hat{x} + \hat{z}$.

Figure 4.2: Quantized wavefront normals.

arrival time at $(x, y, z + dz)$ be $12T$. The wavefront at time $9T$ can then be approximated as $(x, y, z)+(0, 0, (9-8)dz/(12-8)) = (x, y, z+0.25dz)$. Figure 4.3 shows the new wavefronts found using interpolation for this example. Due to this interpolation step, allowable angles are now $\tan^{-1}((M - N)/m)$ which should increase the accuracy of the ray tracing.

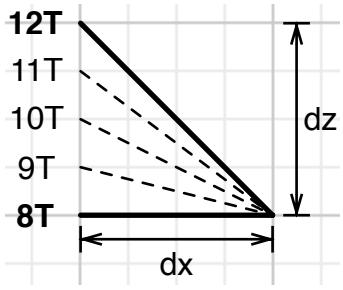

Figure 4.3: Wavefronts found using wavefront interpolation. Wavefronts found without interpolation are shown in bold and additional wavefronts found using interpolation are shown as dashed lines.

4.4 Verification with Snell's Law

In order to validate the ray tracing methods presented above, simulations were performed and then compared to Snell's law. Snell's law states that for

oblique incidence of a plane wave on a planar boundary as shown in Fig. 4.4, $c_2 \sin(\theta_i) = c_1 \sin(\theta_t)$.

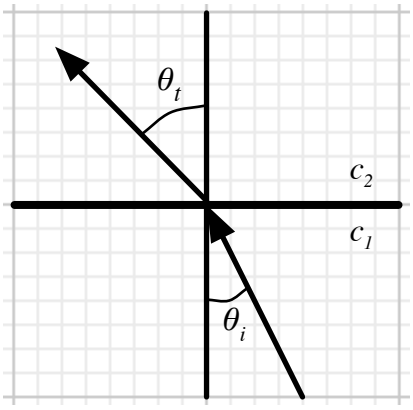

Figure 4.4: Angle and sound speed conventions for Snell's law. θ_i is the angle of incidence, θ_t is the transmission angle, c_1 is the sound speed in the first medium and, c_2 is the sound speed in the second medium.

For the case of the spherical scatterer, the boundary is no longer a plane but can be thought of as a plane tangent to the sphere at the point of intersection of the ray with the sphere as shown in Fig. 4.5. It can be shown that a ray starting at (x, y) and pointing in the $+z$ direction will have an angle of incidence of

$$\theta_i = \sin^{-1}\left(\frac{\sqrt{x^2+y^2}}{r}\right) \tag{4.9}$$

where r is the radius of the sphere. After applying Snell's law, the angle of transmission will then be

$$\theta_t = \sin^{-1}\left(\frac{c_2}{c_1}\frac{\sqrt{x^2+y^2}}{r}\right) \tag{4.10}$$

Define the difference angle θ_d as the difference between θ_t and θ_i,

$$\theta_d = \theta_t - \theta_i \tag{4.11}$$

Since the propagation direction is in the positive z direction, θ_d is the angle between the transmitted ray and the positive z-axis. One can then compute the transmitted ray according to Snell's law as follows. First, compute θ_i, θ_t,

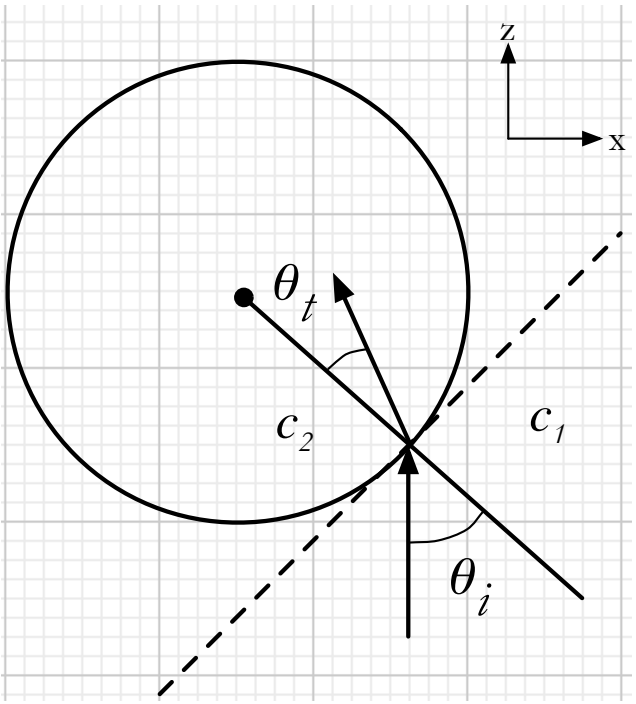

Figure 4.5: Snell's law applied to a plane wave incident on a sphere.

and θ_d as described above. Next, compute the transmitted ray in the $z-x$ plane, which is

$$\mathbf{r_{zx}} = \hat{x}\sin(\theta_d) + \hat{z}\cos(\theta_d) \tag{4.12}$$

The ray must then be rotated about the z-axis by the angle θ_r where

$$\theta_r = \tan^{-1}\left(\frac{y}{x}\right) \tag{4.13}$$

This rotation can be applied using a transformation matrix

$$\begin{bmatrix} r_x \\ r_y \\ r_z \end{bmatrix} = \begin{bmatrix} \cos(\theta_r) & -\sin(\theta_r) & 0 \\ \sin(\theta_r) & \cos(\theta_r) & 0 \\ 0 & 0 & 1 \end{bmatrix} \begin{bmatrix} \sin(\theta_d) \\ 0 \\ \cos(\theta_d) \end{bmatrix} \tag{4.14}$$

where the transformed ray is $\hat{x}r_x + \hat{y}r_y + \hat{z}r_z$. The resulting direction of the transmitted ray according to Snell's law is

$$\mathbf{r_{Snell}} = \hat{x}\sin(\theta_d)\cos(\theta_r) + \hat{y}\cos(\theta_d)\sin(\theta_r) + \hat{z}\cos(\theta_d) \tag{4.15}$$

The error of the ray found with the ray tracing code can now be computed.

First, define a vector $\mathbf{v}$, which is the vector starting at the intersection of the computed ray path with the sphere and ending at some point on the computed ray path after the ray has entered the sphere. The error angle θ_e is then computed by finding the angle between $\mathbf{r_{Snell}}$ and $\mathbf{v}$ using the following equation:

$$\theta_e = \cos^{-1}\left(\frac{\mathbf{r_{Snell}} \cdot \mathbf{v}}{|\mathbf{r_{Snell}}||\mathbf{v}|}\right) \tag{4.16}$$

4.4.1 Verification simulation 1

The first simulation used for verification was a 75 mm diameter sphere with a sound speed of 310 m/s and density of 1.21 kg/m^3 surrounded by a medium with a sound speed of 300 m/s and a density of 1.21 kg/m^3. A 12.5 kHz four-cycle sinusoidal pulse was used. Two renderings of the ray paths are shown in Fig. 4.6. The ray tracing error as a function of angle of incidence is plotted in Fig. 4.7.

4.4.2 Verification simulation 2

The second simulation used for verification was a 75 mm diameter sphere with a sound speed of 330 m/s and density of 1.21 kg/m^3 surrounded by a medium with a sound speed of 300 m/s and a density of 1.21 kg/m^3. A 12.5 kHz four-cycle sinusoidal pulse was used. Two renderings of the ray paths are shown in Fig. 4.8. The ray tracing error as a function of angle of incidence is plotted in Fig. 4.9.

4.4.3 Verification simulation 3

The third simulation used for verification was a 75 mm diameter sphere with a sound speed of 400 m/s and density of 1.21 kg/m^3 surrounded by a medium with a sound speed of 300 m/s and a density of 1.21 kg/m^3. A 12.5 kHz four-cycle sinusoidal pulse was used. Two renderings of the ray paths are shown in Fig. 4.10. The ray tracing error as a function of angle of incidence is plotted in Fig. 4.11. As can be seen from the plot, the error is significantly larger than was observed for the 310 m/s sphere. One factor contributing to this error may be the fact that Snell's law only applies when the wavelength

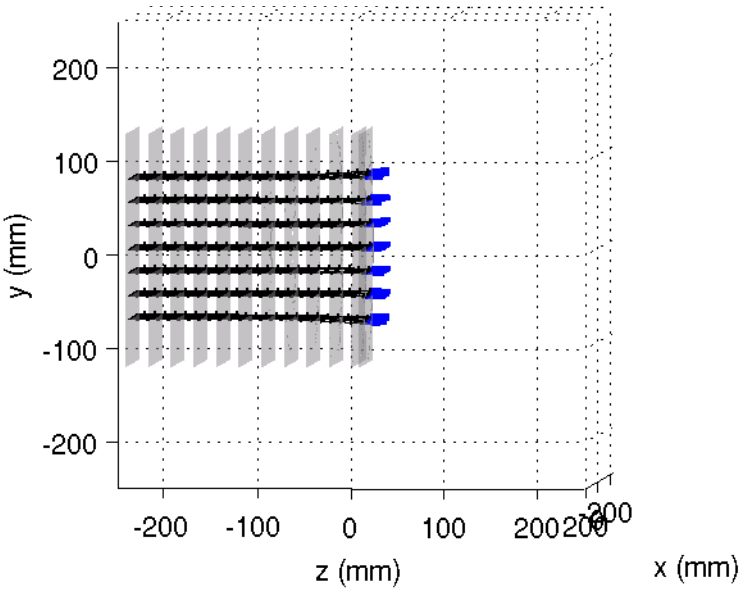

(a) Side View

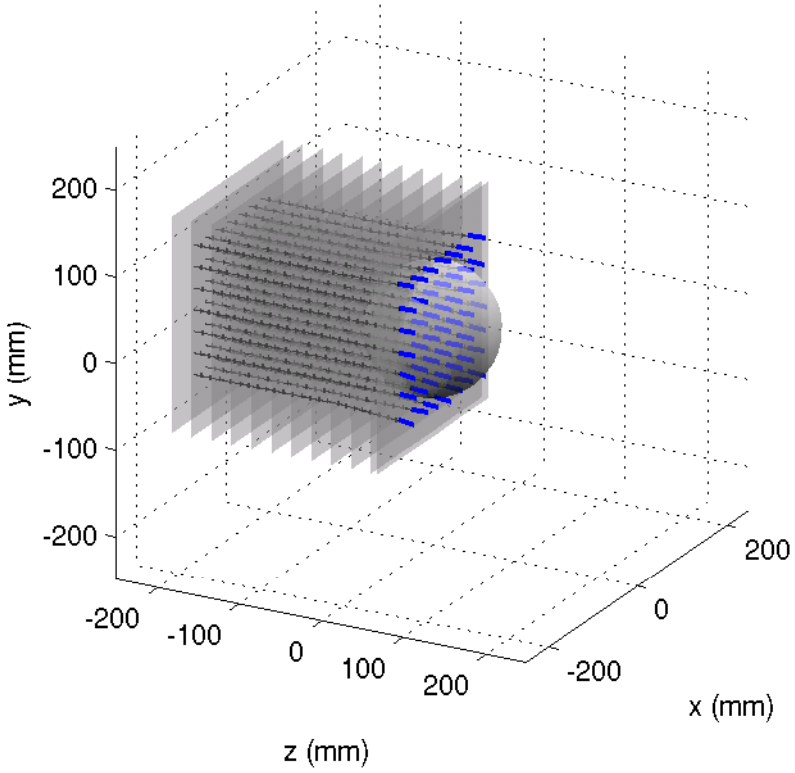

(b) Perspective View

Figure 4.6: Ray tracing for 310 m/s sphere in 300 m/s medium and 12.5 kHz pulse.

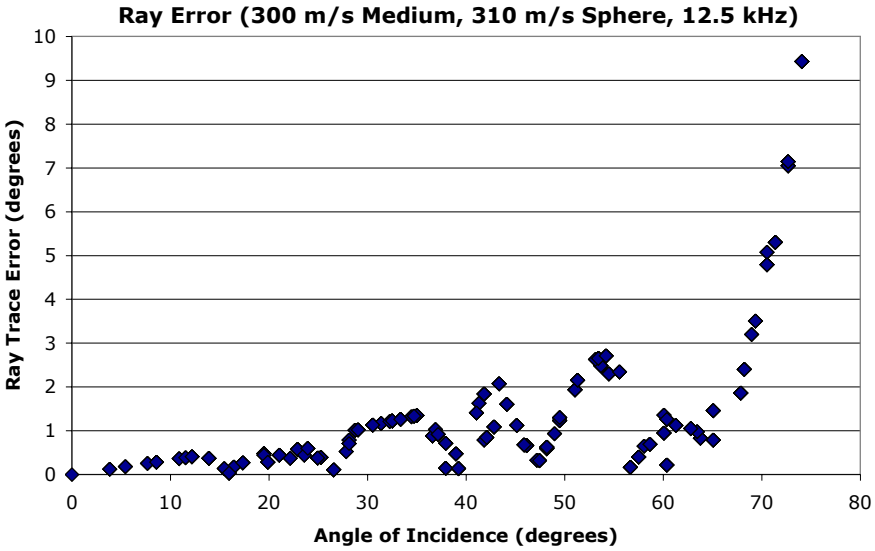

Figure 4.7: Ray tracing error for 310 m/s sphere in 300 m/s medium with matched densities.

approaches zero. In order to verify that this is the source of some of the error, another simulation was performed.

4.4.4 Verification simulation 4

The fourth simulation used for verification was the same as the second except the frequency of the pulse was doubled to halve the wavelength. With this smaller wavelength, the small wavelength assumption of Snell's law should be better satisfied and hence a smaller error observed. Two renderings of the ray paths are shown in Fig. 4.12. The error as a function of the angle of incidence is plotted in Fig. 4.13. Comparison to Fig. 4.11 shows that the error is reduced as the wavelength is made smaller.

4.4.5 Verification simulation 5

The fifth simulation used for verification was a 75 mm diameter sphere with a sound speed of 500 m/s and density of 1.21 kg/m^3 surrounded by a medium with a sound speed of 300 m/s and a density of 1.21 kg/m^3. A 15 kHz four-cycle sinusoidal pulse was used. Two renderings of the ray paths are shown

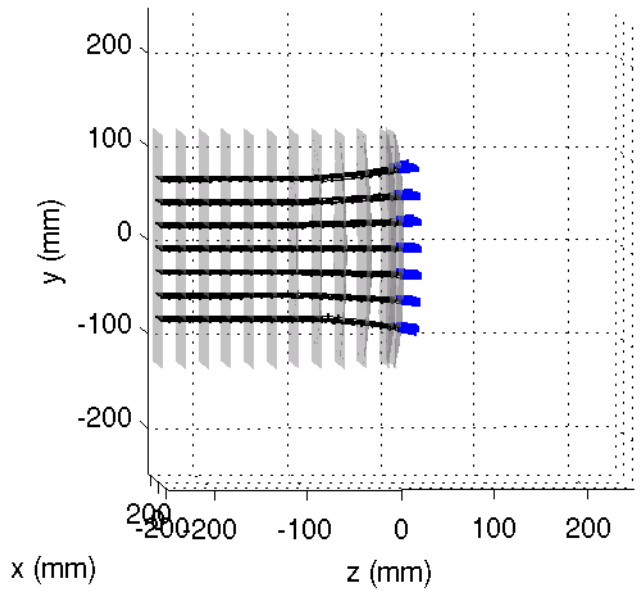

(a) Side View

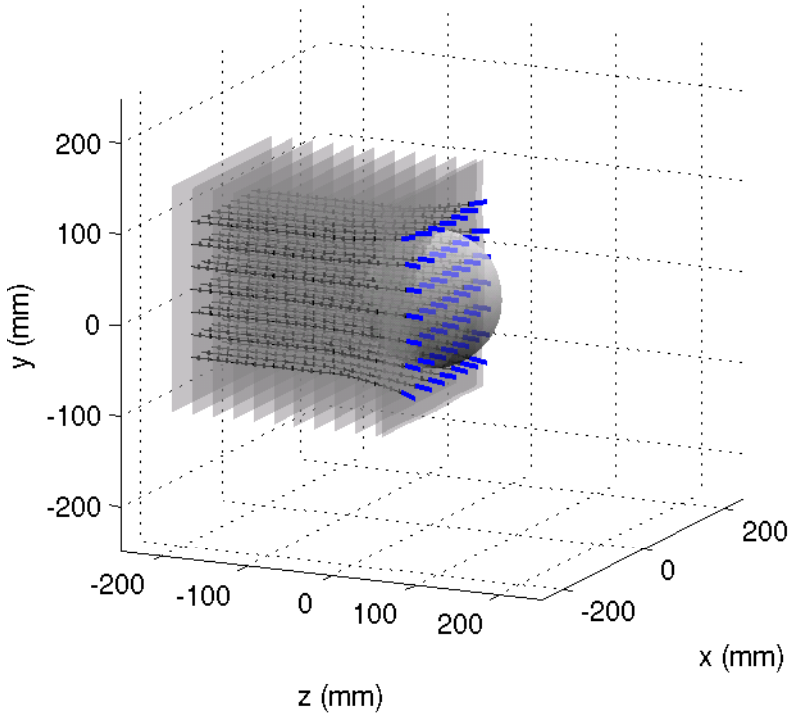

(b) Perspective View

Figure 4.8: Ray tracing for 330 m/s sphere in 300 m/s medium and 12.5 kHz pulse.

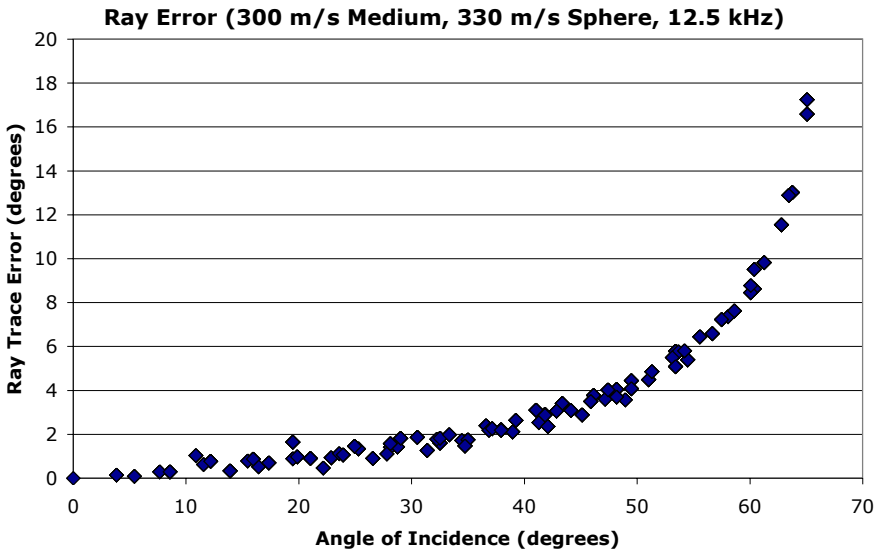

Figure 4.9: Ray tracing error for 330 m/s sphere in 300 m/s medium with matched densities.

in Fig. 4.14. The ray tracing error as a function of angle of incidence is plotted in Fig. 4.15.

4.5 Additional Simulations

4.5.1 Concentric fluid spheres

A simulation was performed using the concentric sphere solution with the properties close to that of the human head. A summary of the values used is shown in Table 4.1. The center frequency of the pulse was 1 kHz. Renderings of the ray tracing at six time steps are shown in Fig. 4.16. Higher resolution versions of these images can be found in the Appendix, Figs. A.1 to A.6. Figure 4.17 shows the rays looking into the $-z$ axis to display the ray concentrations better.

The initial concentration of rays is 16 rays per 400 mm^2 which is shown in Fig. 4.17(a). The second time step is shown in Fig. 4.17(b). Near the bone-air interface the concentration of rays doubles to 32 rays per 400 mm^2, corresponding to having twice the initial intensity in that region. Inside the

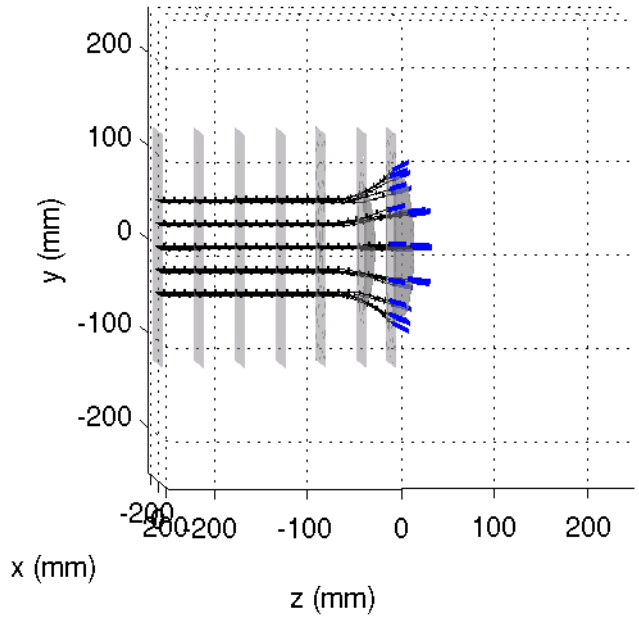

(a) Side View

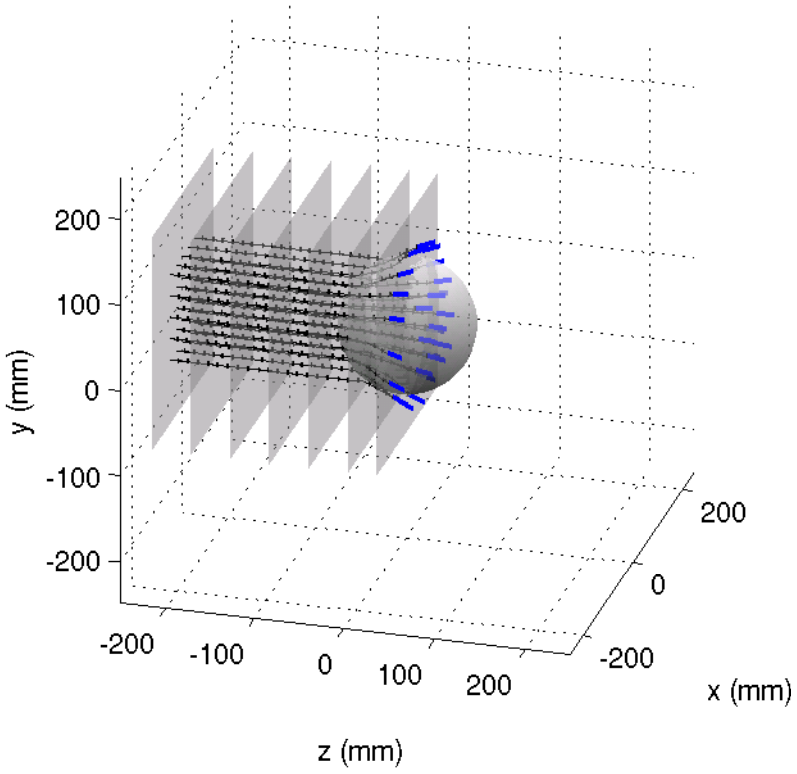

(b) Perspective View

Figure 4.10: Ray tracing for 400 m/s sphere in 300 m/s medium and 12.5 kHz pulse.

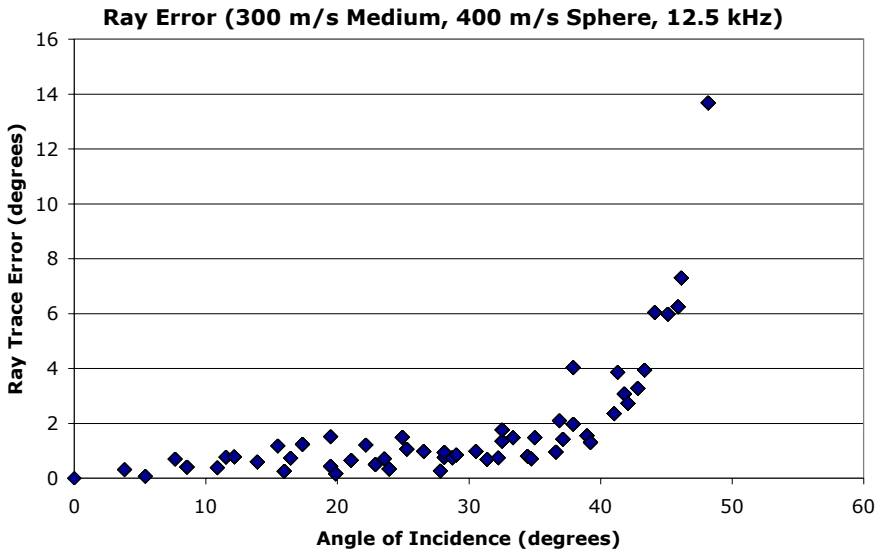

Figure 4.11: Ray tracing error for 400 m/s sphere in 300 m/s medium with matched densities for a 12.5 kHz pulse.

brain region the concentration of rays is reduced by roughly a factor of four to 3 rays per 400 mm^2, corresponding to an intensity that is a quarter of the initial intensity. The third time step is shown in Fig. 4.17(c). Near the bone-air interface the concentration of rays is 31 rays per 400 mm^2 which is still roughly twice the initial concentration. Inside the brain region the concentration of rays is as low as 0.5 rays per 400 mm^2, which has a corresponding intensity of approximately 3% of the initial intensity. The fourth time step is shown in Fig. 4.17(d). Near the bone-air interface the concentration of rays is 28 ray per 400 mm^2, which corresponds to an intensity of 1.75 times the initial intensity. Inside the brain region the concentration of rays is still as low as 0.5 rays per 400 mm^2, which has the corresponding intensity of 3% of the initial intensity. The fifth time step is shown in Fig. 4.17(e). Near the bone-air interface the concentration of rays is 26 rays per 400 mm^2, which corresponds to an intensity of 1.625 times the initial intensity. Inside the brain region the concentration of rays is as low as 1 ray per 400 mm^2, which corresponds to an intensity of approximately 6% of the initial intensity. The sixth time step is shown in Fig. 4.17(f). Near the bone-air interface the concentration of rays is 28 rays per 400 mm^2, which corresponds to an intensity of 1.75 times the initial intensity.

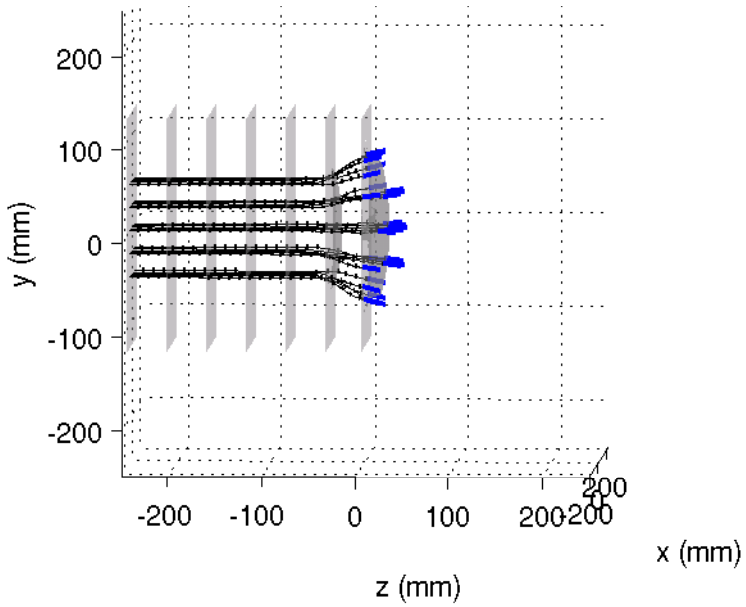

(a) Side View

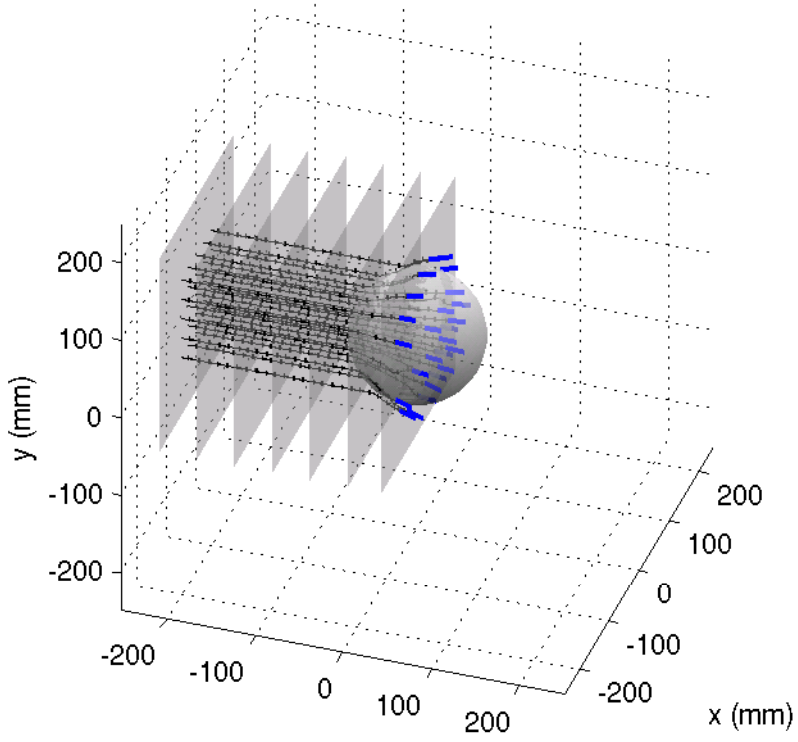

(b) Perspective View

Figure 4.12: Ray tracing for 400 m/s sphere in 300 m/s medium and 24 kHz pulse.

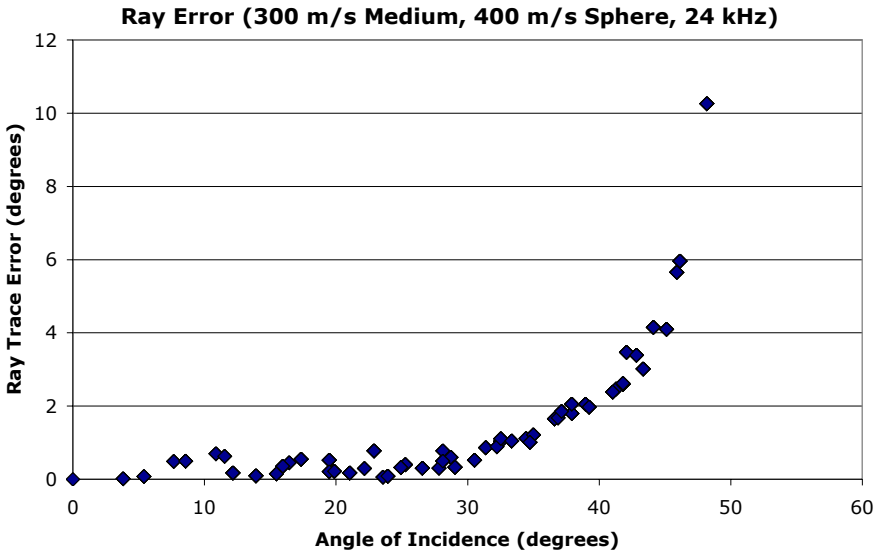

Figure 4.13: Ray tracing error for 400 m/s sphere in 300 m/s medium with matched densities for a 24 kHz pulse.

Table 4.1: Concentric Sphere Simulation Variables.

Region	Radius	c	ρ
Inner Sphere (Brain)	65 mm	1500 m/s	1000 kg/m^3
Outer Sphere (Skull)	75 mm	2900 m/s	2000 kg/m^3
Medium (Air)	N/A	343 m/s	1.21 kg/m^3

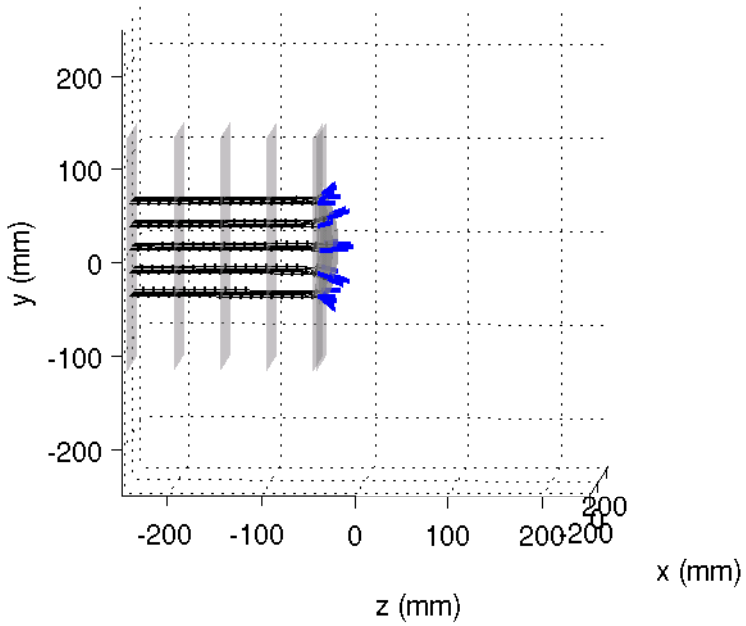

(a) Side View

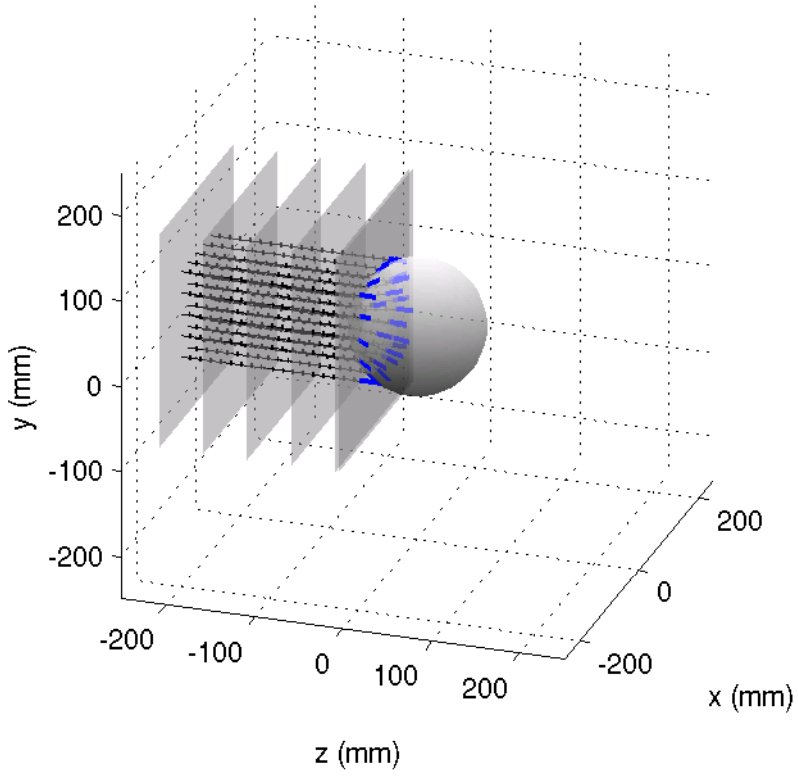

(b) Perspective View

Figure 4.14: Ray tracing for 500 m/s sphere in 300 m/s medium and 15 kHz pulse.

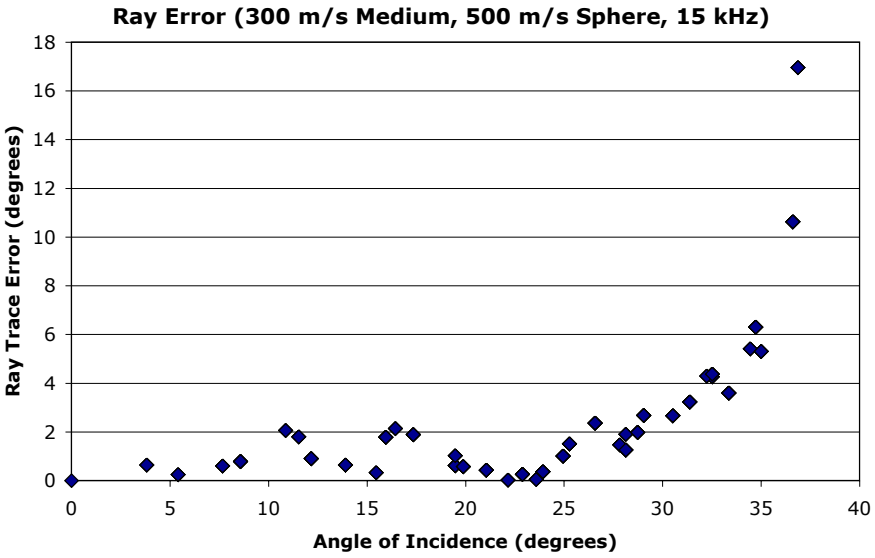

Figure 4.15: Ray tracing error for 500 m/s sphere in 300 m/s medium with matched densities for a 15 kHz pulse.

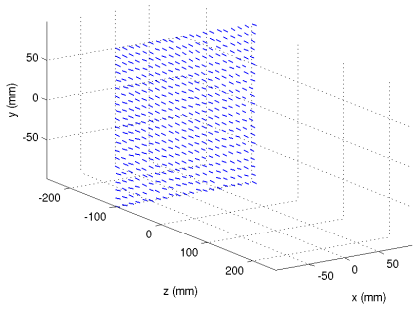

(a) Time: 0.4836 ms

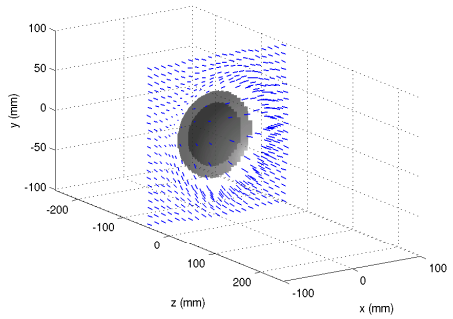

(b) Time: 0.6458 ms

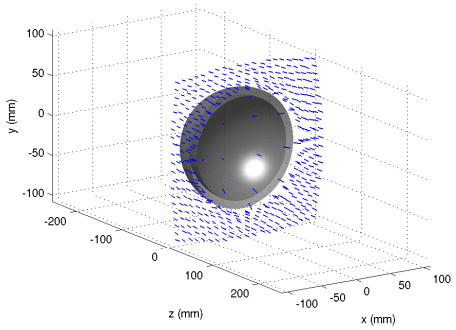

(c) Time: 0.8080 ms

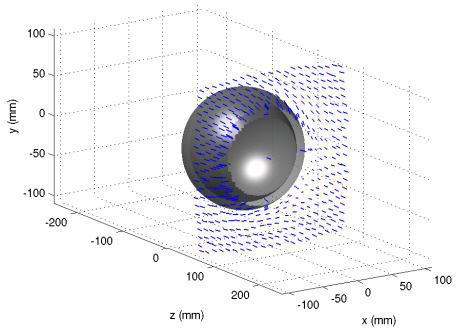

(d) Time: 0.9687 ms

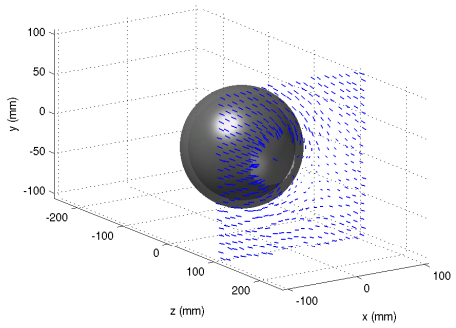

(e) Time: 1.1309 ms

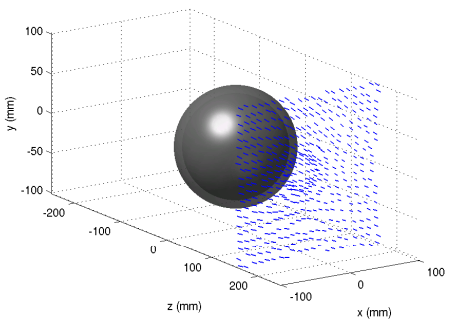

(f) Time: 1.2930 ms

Figure 4.16: Ray tracing for concentric fluid sphere simulation.

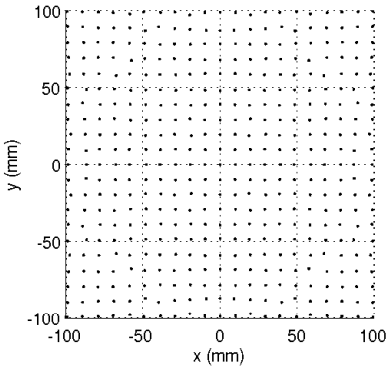

(a) Time: 0.4836 ms

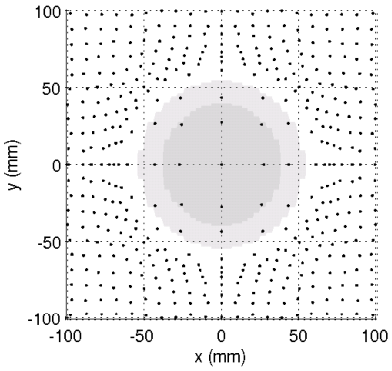

(b) Time: 0.6458 ms

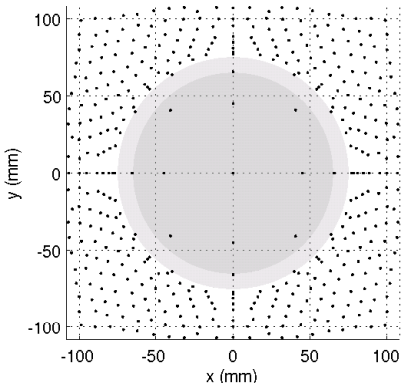

(c) Time: 0.8080 ms

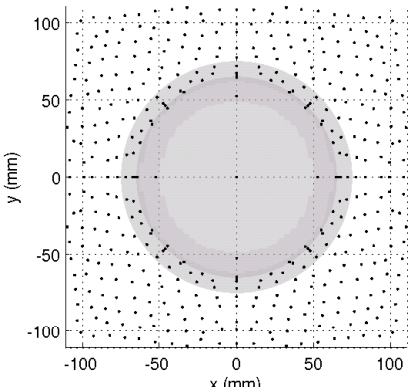

(d) Time: 0.9687 ms

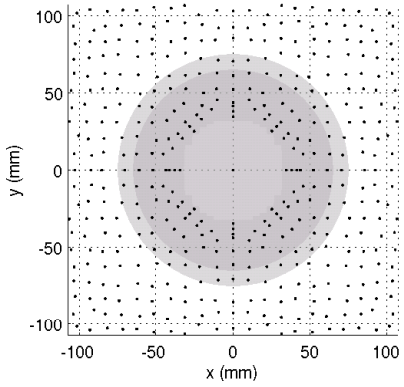

(e) Time: 1.1309 ms

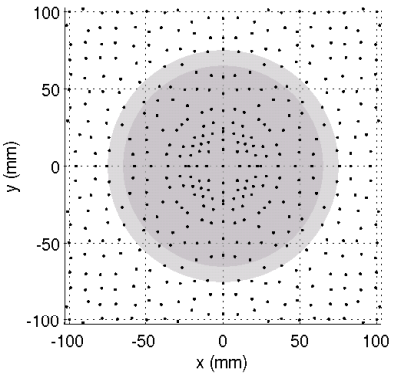

(f) Time: 1.2930 ms

Figure 4.17: Ray concentrations for concentric fluid sphere simulation.